Drug Discoveries & Therapeutics. 2025; 19(3):174-183. *www.ddtjournal.com*

Original Article

DOI: 10.5582/ddt.2025.01041

Immune modulation and improved systemic performance of phosphate-functionalized nanogels for antifungal therapy

Theresa Vogel[1,§], Yidong Yu[2,3,§], Thorsten Keller[1], Atsushi Miyashita[4], Lisa Munakata[5], Ryo Suzuki[5], Andreas Beilhack[3], Jürgen Groll[1], Kazuhisa Sekimizu[6,*], Krystyna Albrecht[1,*]

[1] Department for Functional Materials in Medicine and Dentistry, Institute of Functional Materials and Biofabrication, University of Würzburg, Würzburg, Germany;
[2] JSPS International Research Fellow (Endowed Course "Drug Discoveries by Silkworm Models", Faculty of Pharmaceutical Sciences, Teikyo University, Tokyo, Japan;
[3] Department of Internal Medicine II, Center for Experimental Molecular Medicine, Würzburg University Hospital, Würzburg, Germany;
[4] Institute of Medical Mycology, Teikyo University, Tokyo, Japan;
[5] Laboratory of Drug and Gene Delivery Research, Faculty of Pharmaceutical Sciences, Teikyo University, Tokyo, Japan;
[6] Endowed Course "Drug Discoveries by Silkworm Models", Faculty of Pharmaceutical Sciences, Teikyo University, Tokyo, Japan.

SUMMARY: Phosphate functionalization of nanogels (NGs), originally designed to enhance interactions with fungal pathogens, also significantly influences their immune interactions and systemic behaviour. In this study, we investigated how phosphate-modified NGs perform as antifungal carriers *in vivo* using the silkworm model. We found that phosphate functionalization promotes faster internalization by granulocytes—immune cells functionally similar to mammalian neutrophils—highlighting a trade-off between antifungal activity and immune uptake. In parallel, phosphate-functionalized NGs exhibited prolonged circulation, more consistent biodistribution patterns, and reduced batch variability compared to unmodified NGs. These features contributed to superior and more reproducible *in vivo* antifungal efficacy when delivering itraconazole. Importantly, the biodistribution profiles observed in silkworms aligned well with previous mammalian data, further validating silkworms as an efficient, cost-effective model for early-stage evaluation of nanocarrier systems. Our findings underscore the importance of tuning surface functionalization to balance immune interaction and therapeutic performance, providing valuable insights for optimizing systemic antifungal nanotherapies.

Keywords: antifungal delivery, surface functionalization, silkworm, antimicrobial nanocarriers

1. Introduction

Invasive fungal infections lead to over 2.5 million deaths worldwide each year, posing a major public health challenge further aggravated by the scarcity of effective therapeutic options (*1,2*). Despite the existence of antifungal drugs, their clinical efficacy is often hampered by severe side effects, emerging drug resistance, and limited efficacy (*3*), which underscores a pressing need for improved therapeutic strategies. Nanoparticles (NPs) as drug delivery systems (DDS) offer a promising solution by enhancing local drug concentration, improving bioavailability, and reducing toxicity (*4*). Among NPs, nanoparticulate hydrogels, commonly referred to as nanogels (NGs), are particularly appealing as DDS due to their unique combination of high water content, excellent biocompatibility, versatile chemical properties, and ability to provide controlled drug release (*5*).

Recent advances in NG research have shown potential in delivering antifungal drugs effectively. Our initial research demonstrated that redox-sensitive poly(glycidol) (PG)-based NGs could effectively deliver the model antifungal drug itraconazole (NG-ITZ) to the human fungal pathogen *Aspergillus fumigatus in vitro* under protein-free conditions (*6*). More recently, we found that phosphate functionalization of NGs through quenching with phosphoric acid 2-hydroxyethyl acrylate (PHA), facilitated their interaction with *A. fumigatus* under protein-rich conditions (*7*), likely due to the interaction between the phosphate functional group with chitosan in the fungal cell wall (*8,9*). Furthermore, NG×PHA loaded with itraconazole (NG×PHA-ITZ) exhibited superior therapeutic effects in a silkworm (*Bombyx mori*) model of *A. fumigatus* infection compared to the free drug (*7*). These results suggest NG×PHA's potential for systemic antifungal delivery.

While these findings are promising, they raise additional questions regarding the interactions of NGs with mammalian cells, especially regarding potential cytotoxicity. Although empty NGs and NG×PHA are non-cytotoxic, NG-ITZ and NG×PHA-ITZ exhibit weak cytotoxicity in mammalian cell lines (*6,7*), suggesting that host cells may internalize the drug-loaded NGs—an observation that warrants further investigation. Understanding these interactions is crucial, as the biodistribution of NP-based drug carriers is a key factor influencing their safety and efficacy for clinical applications (*10*). To facilitate systemic antifungal delivery, it is also important to study the biodistribution patterns of NG×PHA within an *in vivo* context.

Conventional preclinical biodistribution studies typically rely on mammalian models, such as mice (*11-14*). However, these mammalian models face significant obstacles, including increasing ethical and regulatory scrutiny and substantial costs. To overcome these challenges during the early stages of nanocarrier development, we utilized the silkworm as an alternative model for preliminary *in vivo* evaluation of antifungal drug-loaded NG×PHA (*7*). The silkworm model delivers several key advantages for preliminary studies, such as minimizing ethical concerns, lowering costs (*15*) and demonstrating effectiveness in the early-stage discovery and development of antimicrobial agents (*16,17*). Furthermore, our previous work demonstrated that the silkworm model can reliably assess the biodistribution and elimination of surface-functionalized gold nanoparticles (AuNPs), providing valuable insights into how surface modifications influence *in vivo* behaviour (*18*).

In this study, we expanded the use of silkworms to compare the cellular interactions and biodistribution of unmodified NGs with NG×PHA, focusing on the impact of phosphate functionalization. We hypothesized that this animal model not only supports the preliminary *in vivo* evaluation of therapeutic effects but also uncovers potential benefits or risks associated with candidate nanocarriers during early development. By using this model, we aim to gain insights into how phosphate functionalization affects NG interactions with host cells and biodistribution, potentially guiding further refinements in NG design for antifungal therapy.

2. Methods

2.1. Synthesis of linear poly(glycidol)

The synthesis of linear poly(glycidol) (PG) with 60 repeating units was carried out following established protocols and characterized accordingly (*7,19,20*). Briefly, the monomer ethoxy ethyl glycidyl ether (EEGE) was synthesized from ethyl vinyl ether and glycidol (*19*). Under inert conditions, the polymerization of EEGE was performed in bulk at 60°C overnight using potassium tert-butoxide as an initiator. The reaction was terminated by the addition of methanol. Subsequently, the obtained poly(EEGE) was deprotected under acidic conditions in tetrahydrofuran (THF), followed by dialysis (for 3 days with 4 water changes per day, using a molecular weight cut-off [MWCO] of 3.5 kDa) and lyophilization, resulting in the formation of linear PG.

2.2. Thiol functionalization of linear PG

Thiol functionalization of linear PG was performed using STEGLICH esterification according to a published method (*21*). Briefly, PG was dissolved in anhydrous *N*,*N*-dimethylformamide (DMF), and 1.1 equivalents of *N*,*N*'-dicyclohexylcarbodiimide (DCC) and 4-dimethylamino pyridine (DMAP) were added. Subsequently, 0.5 equivalents of 3,3′-dithiodipropionic acid (DTPA) in degassed DMF were introduced to the reaction mixture at 0°C. The mixture was stirred at room temperature (RT) overnight. After the formation of the hydrogel, it was washed sequentially with DMF, $CHCl_3$, tetrahydrofuran (THF), EtOH, and water. Then, 0.5 equivalents of tris-(2-carboxyethyl)-phosphine hydrochloride (TCEP·HCl) were added, and the pH of the solution was adjusted to 6-7 with triethylamine (TEA). The reduction was completed after stirring at RT for 4 h. Finally, the thiol-functionalized linear PG (PG-SH) was dialyzed (for 3 days with 4 water changes per day, MWCO = 3.5 kDa) and lyophilized.

2.3. Fluorescence labeling of PG-SH

Fluorescence labeling of PH-SH was performed according to a published method (*6,22*). PG-SH was dissolved in 1× PBS buffer (9 mg/mL). After adding 900 mg of TCEP·HCl, the pH was adjusted to 6 with TEA and the solution was degassed with Argon for 20 min. The labeling reaction was initiated by adding 2 mg of Rhodamine Red C2 maleimide (dissolved in anhydrous DMF at 10 mg/mL). Following an additional 10 min of Argon degassing and overnight stirring at RT, the labeled PG-SH was purified *via* dialysis (3 days, with 4 water changes per day, MWCO = 3.5 kDa) and then lyophilized.

2.4. Synthesis of nanogels *via* nanoprecipitation

Nanogels (NGs) were prepared using a nanoprecipitation technique involving linear PG-SH (with or without fluorescent labeling) in acetone, as previously described (*6,7*). Briefly, 6 mg of the respective polymer was dissolved in water (6 mg/90 µL) and precipitated in 48 mL of acetone with an automatic pipette (Eppendorf®-Xplorer). After 30 min, 30 µL of alloxan monohydrate solution in water (32 mg/mL) was added. The oxidation was halted by adding 4 mL of Milli-Q water after another 30 min.

The nanogels were separated from the precipitation solution by centrifugation at 4000× *g*, at RT for 60 min. The samples were washed five times with water by centrifugation (16162× *g*, RT, 5 min [3×], 2.5 min [2×]). The particle size, zeta-potential, and particle concentration of the NGs were then measured.

2.5. Phosphate functionalization of nanogels

NGs were functionalized by incorporating a quenching step into the previously described synthesis procedure (*7*). After the oxidation step, the pH of the solution was adjusted to 8-9 using TEA. Subsequently, 50 µL of quencher (PHA in acetone at 0.283 mg/mL, 3.49 mmol) was added. Quenching was conducted at RT for 30 min. Following this step, the washing and characterization procedures were carried out as described earlier.

2.6. Rearing of silkworms (*Bombyx mori*)

Silkworm eggs (strain: Kinsyu × Showa) were purchased from Ehime-Sanshu (Ehime, Japan). After hatching, the larvae were reared at 27°C and nourished with an artificial diet (Silkmate 2S, Nosan Corporation, Japan) until the fourth instar. Upon reaching the fifth instar, the larvae were switched to an antibiotic-free diet (Artificial diet for silkworm larvae, Type A, Sysmex Corporation, Japan) for two days (1 g diet/silkworm/day). On the third day of the fifth instar, silkworms were used for experiments unless otherwise specified.

2.7. Collection of hemolymph from silkworms

On the third day of the fifth instar, hemolymph was collected from silkworms under sterile conditions. For surface disinfection, silkworms were soaked in 70% EtOH for 10 min at RT, followed by a brief air-drying period. Hemolymph was then collected by cutting one of the abdominal legs. To prevent melanization, N-phenylthiourea (PTU; 0.1 M in 100% DMSO) was immediately added to the collected hemolymph to achieve a final concentration of 1 mM (*23*). The hemolymph was then centrifuged at 16162 × g, for 1 min at 4°C to pellet the hemocytes. The supernatant was used as a culture medium (*i.e.*, cell-free hemolymph) on the same day of collection or stored at -20°C for further use.

For MIC (minimal inhibitory concentration) determination or characterization of protein corona formation, a larger volume of cell-free hemolymph was required. In this case, silkworms were fed for four days, and hemolymph was collected on the fifth day of the fifth instar.

2.8. Interaction of NGs with primary adherent hemocytes from silkworms

On the third day of the fifth instar, hemolymph was collected from silkworms as described earlier. PTU was added, and 250 µL of hemolymph was immediately transferred into a glass-bottom dish (ø 35 mm [dish]; ø 14 mm [cover slip; poly-lysine coated]; Matsunami, Osaka, Japan), and the cells were allowed to settle for 30 min at RT. Subsequently, the hemolymph was removed, and the cells were washed twice with TC-100 insect medium containing 8% heat-inactivated fetal bovine serum (FBS), 40 IU/mL of penicillin-streptomycin, and 0.1% w/v PTU (250 µL medium per wash). The adherent hemocytes, consisting of granulocytes and plasmatocytes, were obtained (*24*).

Following the second wash, fresh TC-100 medium containing 4×10^9 particles of the desired NG type was added to each dish (250 µL/dish). The samples were co-incubated at 27°C for 1, 3, 6, or 24 h. After co-incubation, the samples were washed five times with 300 µL of Dulbecco's phosphate-buffered saline (DPBS[-]) per wash. Calcein-AM staining was then performed according to the manufacturer's protocol, using a 1 mM stock solution in 100% DMSO with a final concentration of 0.667 µM in 300 µL DPBS(-) per dish. Staining was done in the dark at 27°C for 15 min, followed by three washes as described above. Finally, 100 µL of DPBS(-) was added to each sample, which was then subjected to microscopic examination using a Leica DMI 6000 B fluorescence microscope.

2.9. Biodistribution experiments

To study the biodistribution of NG or the free dye RhoRC2 in silkworms following systemic administration (*i.e.*, intra-hemolymph injection), seven time points were selected: immediately post-injection (0 h), 15 min, 1 h, 3 h, 6 h, 15 h, and 24 h post-injection. For the later time points (15 h and 24 h), silkworms were fed for two days and injected on the third day of the fifth instar. For the other time points, silkworms were fed for two days and fasted for one day prior to the injection. The body weight of individual silkworms (2.1 ± 0.1 g) was recorded prior to injection. Hemolymph and tissue collection occurred on the fourth day of the fifth instar for all seven time points.

A total of 8×10^9 particles of the desired NG batch (or 1.2 µg of the free dye RhoRC2) in 50 µL of DPBS(-) were injected into the hemolymph of individual silkworms as previously described (*25*). The silkworms were incubated at 27°C until dissection. Hemolymph and tissue collection (midgut, Malpighian tubules, hindgut, and fat body) was performed as described earlier and in the Appendix A. Supplementary information (*https://www.ddtjournal.com/action/getSupplementalData.php?ID=257*) (see section "Standard curves of each fluorescently labeled NG batch and the free dye RhoRC2 in distinct silkworm tissues"), respectively. To obtain sufficient tissue homogenates for measuring fluorescent intensity in technical triplicates, hemolymph and respective tissues from 3-5 silkworms were pooled together (defined as 1 biological replicate). Unless otherwise specified, biological duplicates per NG batch were subjected to measurement. Tissue homogenization was carried out as described in the Appendix A. Supplementary information (*https://www.ddtjournal.com/action/getSupplementalData.php?ID=257*) (see section "Standard curves of each fluorescently labeled NG batch and the free dye RhoRC2 in distinct silkworm tissues"). 100 µL of hemolymph (containing hemocytes) or tissue homogenate was used for measuring fluorescent intensity in technical triplicates.

Using GraphPad Prism (v. 8.4.3), non-linear fitting was applied to model the retention kinetics and estimate Terminal half-lives ($t_{1/2}$). A one-phase decay model was used for RhoRC2-NG and free RhoRC2 dye to represent a single, continuous decay process. In contrast, a two-phase decay model was applied for RhoRC2-NG×PHA, reflecting both an initial rapid decline and a slower terminal phase in retention. To assess batch consistency within each NG type, an extra sum-of-squares F test was performed, comparing the decay rate parameters across the three batches. Data are presented as the mean ± SEM for each time point, based on all six replicates (biological duplicates x technical triplicates).

In general, the results on tissue retention are shown as percentages of initial dose (ID) injected per milligram of tissue (% of ID / mg tissue), calculated as follows:

$$\frac{\%\ \text{of ID}}{mg_{tissue}} = \frac{p_{100\mu L}}{p_{ID} \cdot \%h} \qquad (1)$$

where p_{ID} is 8×10^9 particles or 1.2 µg of the free dye (initial dose), $p_{100\mu L}$ is the number of particles or amount of the free dye (ng) in 100 µL of the tissue homogenate (estimated based on respective standard curves, see Appendix B (*https://www.ddtjournal.com/action/getSupplementalData.php?ID=258*). Summary of raw data and standard curves), *%h* is the percentage of tissue in the homogenate, calculated as follows:

$$\%h = \frac{w_{tissue}}{w_{tissue} + w_{saline}} \qquad (2)$$

where w_{tissue} is the weight of the collected tissue, w_{saline} is the weight or volume of saline added for homogenization (density = 1 mg/µL). Data are summarized in the Appendix C (*https://www.ddtjournal.com/action/getSupplementalData.php?ID=259*). Summary of tissue retention data and collectively presented in Figure 4.

3. Results

3.1. Synthesis of phosphate-functionalized, fluorescently labelled NGs for cellular interaction and biodistribution studies

NGs were synthesized from thiol-functionalized poly(glycidol) (PG-SH) *via* nanoprecipitation (Figure 1A) (*6,7*). To achieve phosphate functionalization, we added a quenching step with PHA into the synthesis to introduce a phosphoric acid functional group, resulting in NG×PHA (Figures 1A-1B) (*7*). For tracking cellular interactions and biodistribution, we pre-labeled PG-SH with the maleimide-functionalized dye Rhodamine Red C2 (RhoRC2) prior to NG synthesis (Figure 1C). For biodistribution experiments, we selected RhoRC2 due to its structural similarity to rhodamine B, which has been used for NP biodistribution research in mice (*13*) and for studying xenobiotics in silkworms (*26*). RhoRC2 shares a comparable excitation/emission spectrum to rhodamine B (~560/580 nm) and forms covalent bonds with PG-SH. We synthesized and characterized three batches of RhoRC2-NG and RhoRC2-NG×PHA (Table S1, Appendix A. Supplementary information, *https://www.ddtjournal.com/action/getSupplementalData.php?ID=257*).

3.2. Enhanced interaction of granulocytes with phosphate-functionalized NGs compared to unmodified NGs

First, we co-incubated both NG types with *A. fumigatus* in protein-rich (cell-free hemolymph collected from silkworms) and protein-free (RPMI-1640) media. In protein-rich conditions, only RhoRC2-NG×PHA interacted with the fungus, while both NG types adhered to the fungus in protein-free conditions (Figure S1, Appendix A. Supplementary information, *https://www.ddtjournal.com/action/getSupplementalData.php?ID=257*), consistent with our previous findings (*7*).

After confirming the interaction between NG×PHA with *A. fumigatus*, we assessed how NGs interacted with host cells. To align with our subsequent biodistribution studies in the silkworm model, we selected primary adherent hemocytes isolated from silkworm hemolymph (*24*) as representative host cells. These hemocytes, which include granulocytes and plasmatocytes and constitute over 50% of circulating hemocytes (*24,27*), play a crucial role in the initial cellular response to foreign materials (*28*). Their key role in immune defence makes them well-suited for *in vitro* studies designed to mimic the *in vivo* environment following systemic NG administration.

To assess interactions with host cells, we incubated primary adherent hemocytes from hemolymph with both NG types and the free dye RhoRC2 for either 1, 3, 6, or 24 h (Figure 2; Figures S2-S4, Appendix A. Supplementary information, *https://www.ddtjournal.com/action/getSupplementalData.php?ID=257*). Cell viability, assessed with Calcein-AM staining post co-incubation, remained unaffected. Free dye was primarily detected extracellularly, indicating that the intracellular RhoRC2 signal resulted from the cellular NG uptake. Round-shaped granulocytes internalized RhoRC2-NG×PHA more rapidly than RhoRC2-NG, with marked uptake noted after 3 h of co-incubation (Figure 2).

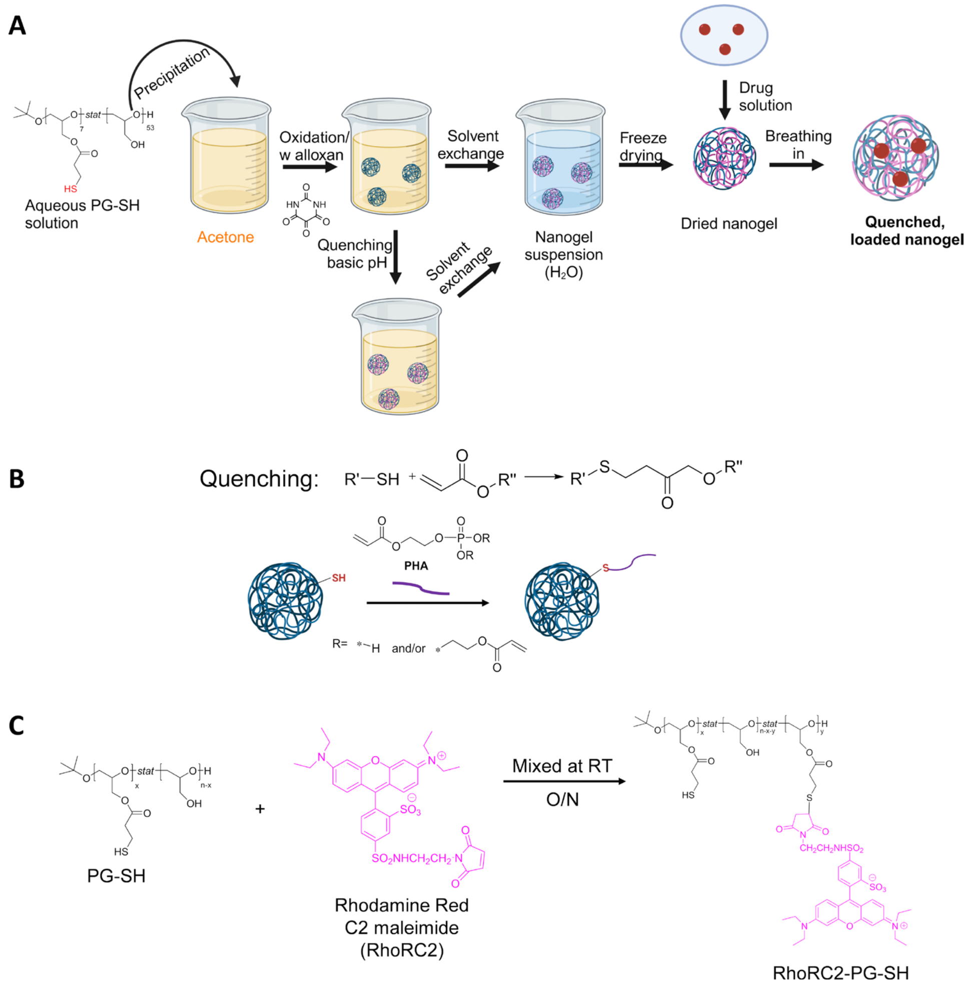

Figure 1. (**A**) Scheme of nanogel (NG) synthesis *via* inverse nanoprecipitation, including functionalization *via* quenching and drug loading steps (image reproduced from Vogel *et al*. 2024 (*7*) under the Creative Commons CC-BY-NC license). (**B**) Detailed illustration of the quenching step (image adapted from Vogel *et al*. 2024 (*7*); icons were created with BioRender under a publication license). (**C**) Fluorescent labeling of PG-SH with Rhodamine Red C2 maleimide. PG-SH: thiol-functionalized poly(glycidol); PHA: phosphoric acid 2-hydroxyethyl acrylate; RT: room temperature; O/N: overnight.

Discrete uptake of RhoRC2-NG by granulocytes was noted after 6 h (Figure S3, *https://www.ddtjournal.com/action/getSupplementalData.php?ID=257*), which became more apparent after 24 h (Figure S4, *https://www.ddtjournal.com/action/getSupplementalData.php?ID=257*). Plasmatocytes (elongated cells) exhibited minimal uptake in both cases.

Notably, both NG types are likely degraded within granulocytes due to ester hydrolysis under the acidic conditions (*19*), although RhoRC2 remains detectable due to its pH stability (*29*).

3.3. Prolonged circulation of phosphate-functionalized NGs in silkworm hemolymph

After completing the *in vitro* study, we conducted *in vivo* biodistribution experiments. We systemically administered RhoRC2-NG, RhoRC2-NG×PHA, or free dye RhoRC2 to silkworms At seven time points within 24 h – 0 h (immediately after injection), 15 min, 1 h, 3 h, 6 h, 15 h, and 24 h – we collected hemolymph (the silkworm equivalent of vertebrate blood (*30*)) and four tissue types (midgut, Malpighian tubules, hindgut, and fat body).

To prevent NG pelleting, we analyzed hemolymph without centrifugation. Using RhoRC2 signals (Figure 3), we estimated NG half-lives in hemolypmh, defined as the time for plasma concentration to drop by 50% during the terminal phase (*31*). Both the free dye RhoRC2 (Figure 3C) and RhoRC2-NG (Figure 3A) followed a one-phase decay model, with half-lives of 3.5 h and 2.0-6.6 h, respectively, indicating relatively rapid clearance from the hemolymph. In contrast, RhoRC2-NG×PHA (Figure 3B) exhibited a two-phase decay model, characterized by an initial rapid decline followed by a prolonged terminal phase with half-lives ranging from 9.5 to 19.9 h. This extended half-life of RhoRC2-NG×PHA may result from faster uptake by granulocytes, as demonstrated in *in vitro* co-culture experiments where RhoRC2-NG×PHA showed more pronounced intracellular accumulation than RhoRC2-NG, persisting for at least 6 h (Figure 2, Figures S2-S3). Interestingly,

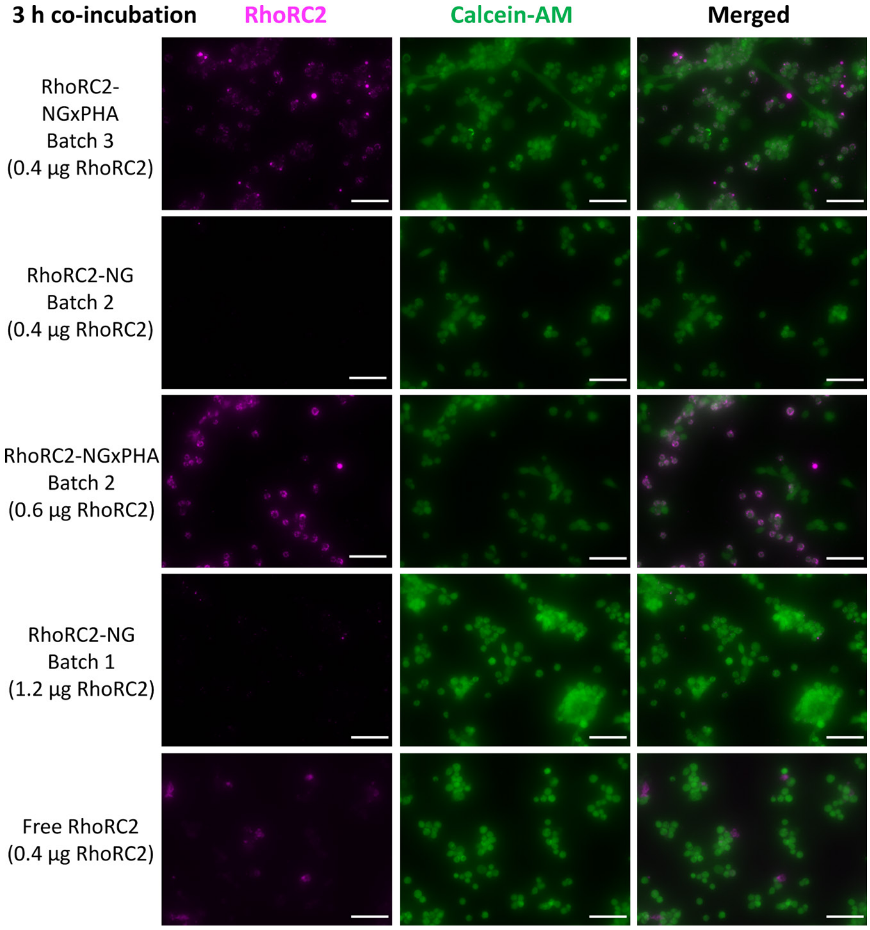

Figure 2. Co-incubation of two distinct NG types with primary adherent hemocytes (granulocytes and plasmatocytes) collected from silkworms for 3 h at 27°C in 250 µL TC-100 medium containing 8% FBS. Two batches of each NG type, as indicated in Table S1 (Appendix A. Supplementary information, *https://www.ddtjournal.com/action/getSupplementalData.php?ID=257*), were used. A total of 4×10^9 particles from each batch were added to respective wells for co-incubation. Given the slightly variations in estimated RhoRC2 loading among the batches, the amount of RhoRC2 in each well was indicated in parentheses. Free dye was used as a control. Following co-incubation, hemocytes were stained with Calcein-AM to confirm their viability. Scale bars = 50 µm.

while the free dye stabilized at approximately 40% of its initial signal by 24 h post injection, both NG types decreased to approximately 10-20%. These findings suggest that, despite initial differences in retention, NGs undergo more efficient clearance from circulation than the free dye during the terminal phase.

3.4. Tissue-specific retention of NGs in silkworms

Tissue retention analysis revealed that both NG types (Figures 4A-4B) predominantly localized in the midgut (akin to the mammalian small intestine (*32*), which also metabolizes exogenous compounds like the liver (*33*)) and the hindgut (comparable to the mammalian large intestine (*34*)). Smaller amounts accumulated in the fat body (responsible for energy storage, metabolism, and partial detoxification, often likened to the mammalian liver (*15*)). The Malpighian tubules (similar to mammalian kidneys (*15*)) showed the least retention. In contrast, the free dye displayed a distinct retention pattern, with primary accumulation in the Malpighian tubules and minimal retention in the hindgut (Figure 4C).

Given the hemolymph retention profiles (Figure 3), we focused our tissue retention analysis on two time points: 3 h post-injection to capture early biodistribution, and 24 h to assess longer-term retention and potential tissue accumulation. At 3 h, RhoRC2-NG (Figure 4A) accumulated significantly more in the midgut than in the fat body and Malpighian tubules. Similarly, RhoRC2-NG×PHA (Figure 4B) displayed greater retention in the midgut than in the fat body, Malpighian tubules, and hindgut. By 24 h, RhoRC2-NG continued to show higher retention in the midgut relative to the other two tissues. However, RhoRC2-NG×PHA no longer exhibited significant differences between the midgut and fat body or hindgut, although retention in the midgut remained higher than in the Malpighian tubules. The free dye (Figure 4C) displayed a distinct retention profile, with significantly higher accumulation in the Malpighian tubules compared to the midgut at 3 h. This difference disappeared by 24 h, indicating clearance over time. Overall, comparisons between tissue types at these time points revealed a clear trend: both NG types preferentially accumulated in the midgut early on, while

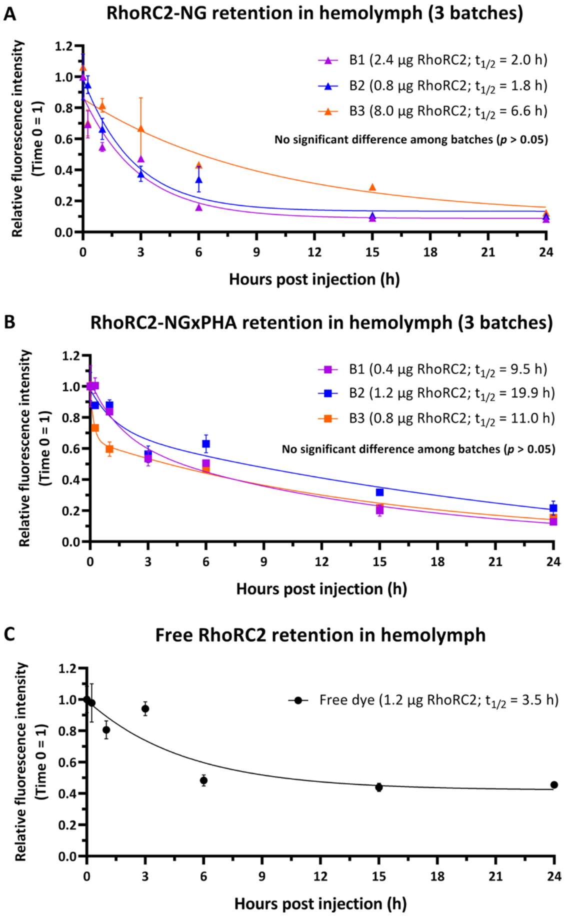

Figure 3. Retention of two distinct NG types in silkworm hemolymph post systemic administration. Three batches (B1, B2, B3) of RhoRC2-NG (**A**) and RhoRC2-NG×PHA (**B**) as well as the free dye RhoRC2 (**C**) were used. A total of 8×10^9 particles of each NG batch were injected into individual silkworms, followed by collection of hemolymph at indicated time points. Given the slight variations in estimated RhoRC2 loading among the NG batches, the amount of RhoRC2 injected into each silkworm is indicated in the parentheses in the legend. Fluorescence intensities were normalized to the initial time point (0 h) to adjust for loading variability, allowing comparison of relative retention profiles. Terminal half-lives ($t_{1/2}$) in hemolymph (containing hemocytes) were estimated using a one-phase decay model for RhoRC2-NG (**A**) and free RhoRC2 (**C**), while a two-phase decay model was used for RhoRC2-NG×PHA (**B**); these values are shown in parentheses in the legend. Notably, based on the observed batch variations, the half-life of NGs appears to be positively related to the injected amount of RhoRC2. An extra sum-of-squares F test revealed no significant retention differences among batches within each NG type ($p > 0.05$). Measurements were performed in biological duplicates (pooled hemolymph from 3–5 silkworms per sample), with each sample measured in technical triplicates. Data represent the mean ± SEM for each time point, based on all six replicates.

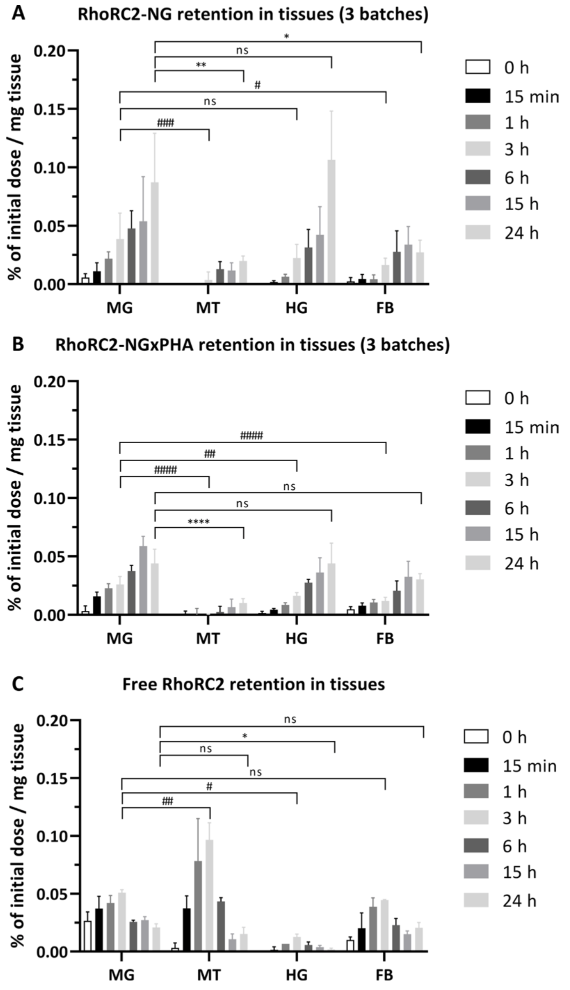

Figure 4. Tissue retention of two distinct NG types in silkworms following systemic administration. Three batches of RhoRC2-NG (**A**) and RhoRC2-NG×PHA (**B**) were injected, along with a free dye control, RhoRC2 (**C**). Each silkworm received 8×10^9 particles for NG or 1.2 μg of free dye, and tissues were collected at the specified time points. Data represent mean ± SD from biological duplicates (pooled tissues from 3–5 silkworms per sample) across all three batches (except for the free dye control), with each sample measured in technical triplicates. Abbreviations: MG (midgut), MT (Malpighian tubules), HG (hindgut), FB (fat body). Statistical comparisons were conducted at two key time points (3 h and 24 h post injection) using one-way ANOVA followed by Dunnett's multiple comparisons test, comparing MT, HG, and FB to MG at each respective time point. Significance indicators: $^{*/\#}p < 0.05$; $^{**/\#\#}p < 0.01$; $^{***/\#\#\#}p < 0.001$; $^{****/\#\#\#\#}p < 0.0001$; ns (not significant).

the free dye showed stronger retention in the Malpighian tubules.

3.5. Distinct protein corona profiles of phosphate-functionalized and unmodified NGs

To investigate the prolonged retention of RhoRC2-NG×PHA in hemolymph compared to RhoRC2-NG, likely due to enhanced granulocyte uptake, we incubated unlabeled NGs and NG×PHA in hemolymph for 24 h. After incubation, both types displayed similar particle sizes and zeta potentials after incubation (Table S2, Appendix A. Supplementary information, *https://www.ddtjournal.com/action/getSupplementalData.php?ID=257*).

Next, we explored NG interactions with hemolymph proteins by analyzing the protein corona composition after a 24 h incubation of unlabeled NGs or NG×PHA. Liquid chromatography coupled with mass spectrometry (LC-MS/MS) identified proteins < 200 kDa, constituting 96% of the corona for both NG types (Figure S5A, Appendix A. Supplementary information, *https://*

www.ddtjournal.com/action/getSupplementalData.php?ID=257); Appendix D (*https://www.ddtjournal.com/action/getSupplementalData.php?ID=260*). Full list of hard corona proteins on NGs). As shown in Figure S5B (*https://www.ddtjournal.com/action/getSupplementalData.php?ID=257*), differences in the most abundant proteins included higher proportions of C-type lectin domain proteins on NGs, critical for innate immunity (*35*) (48.3% of total identified proteins on NGs *vs*. 26.3% on NG×PHA). Conversely, there were lower proportions of nutrient storage proteins on NGs, which are abundant in hemolymph (*36*) (24.8% on NGs and 41.4% on NG×PHA). Among them, lipid-binding proteins, particularly apolipophorins and low molecular weight lipoproteins (*36*), accounted for 8.61% on NGs and 24.41% on NG×PHA (Table S3, Appendix A. Supplementary information, *https://www.ddtjournal.com/action/getSupplementalData.php?ID=257*). Other proteins comprised 26.9% and 32.3% of total quantities, respectively.

We identified two low molecular weight lipoproteins (LPs), 30KP2 (BmLP7) and PBMHP-6 (BmLP1), among the lipid-binding proteins that might affect NG×PHA's interaction with granulocytes. BmLP7, which appeared only on NG×PHA (1.04%), can penetrate hemocytes, while BmLP1, more abundant on NG×PHA than NGs (13.62% *vs.* 5.52%), can recruit hemocytes to BmLP1-coated substances (*37*). These differences likely facilitate NG×PHA's interaction with hemocytes *in vivo*.

3.6. Phosphate-functionalized NGs as reliable antifungal carriers with reduced batch variability and improved efficacy

In our initial study, itraconazole-loaded NGs (NG-ITZ) exhibited a lower minimal inhibitory concentration (MIC) against *A. fumigatus* in a protein-free medium compared to free itraconazole (ITZ) (*6*). Since NGs do not interact with the fungus in protein-rich conditions (Figure S1A, *https://www.ddtjournal.com/action/getSupplementalData.php?ID=257*) (*7*), we did not expect any antifungal effects of NG-ITZ under such conditions. However, after observing similar biodistribution patterns between empty NGs and NG×PHA, we decided to reassess NG-ITZ.

We determined the MIC and median effective dose (ED_{50}) of NG-ITZ against *A. fumigatus*, comparing these results with previous data on NG×PHA-ITZ and free ITZ (*6, 7*). NG-ITZ (two batches tested) exhibited ED_{50} values of 1.9 and 2.1 mg/kg larva, slightly higher than those of NG×PHA-ITZ (two batches, both 1.3 mg/kg larva), and consistent with the corresponding MIC values in silkworm hemolymph (2-4 µg/mL for NG-ITZ *vs*. 1 µg/mL for NG×PHA-ITZ (Table S4, Appendix A. Supplementary information, *https://www.ddtjournal.com/action/getSupplementalData.php?ID=257*). The MIC values in RPMI was also in line with these trends (1 µg/mL for NG-ITZ *vs*. 0.5 µg/mL for NG×PHA-ITZ). Importantly, NG-ITZ demonstrated better *in vivo* antifungal effect than free ITZ (ED_{50} > 4.7 mg/kg larva), though not as effective as NG×PHA-ITZ. Moreover, NG-ITZ exhibited greater batch variability in antifungal effects compared to NG×PHA-ITZ, underscoring NG×PHA's potential as a more consistent and reliable antifungal drug carrier, with enhanced fungal interaction and improved biodistribution.

4. Discussion

Phosphate functionalization of NGs enhances their interactions with fungi and promotes faster internalization by silkworm granulocytes, which are similar to mammalian neutrophils and play a key role in the initial recognition of foreign materials (*38,39*). This dual effect strikes a balance between improved antifungal activity and increased immune cell uptake, illustrating the trade-off in systemic antifungal delivery strategies. Notably, both unmodified and phosphate-functionalized NGs selectively interact with granulocytes, rather than the plasmatocytes, emphasizing their potential for immune-specific targeting. The accelerated internalization of phosphate-functionalized NGs further underscores their enhanced functionality, suggesting broad applications, including optimizing drug delivery to specific immune cell populations.

While the biodistribution patterns of PG-SH-based NGs in animal models remain limited, our findings (Figures 4A-4B) align with previous data on Cy7-labeled PG-SH-based NGs in mice (Cy7-NG×HEA quenched with 2-hydroxyethyl acrylate) (*12*). *In vivo* imaging in mice, particularly at 3 h post injection, revealed that Cy7-NG×HEA was primarily cleared *via* hepato-biliary excretion (liver and intestine) rather than renal clearance (kidneys and bladder), likely due to the NG's particle size (*12*). The similarity in biodistribution patterns between silkworms and mice reinforces the silkworms as a reliable and cost-effective tool for initial nanocarrier biodistribution studies.

Our findings further demonstrate that NG×PHA-ITZ delivers superior *in vivo* antifungal effects with less variability compared to NG-ITZ (Table S4, *https://www.ddtjournal.com/action/getSupplementalData.php?ID=257*), highlighting NG×PHA as a promising nanocarrier. However, additional optimization is necessary to achieve fungal-specific drug delivery, as phosphorylation alone may not suffice. Future research will focus on quantifying the degree of phosphorylation in NG×PHA, exploring its tunability, and examining its impact on biodistribution. This could offer valuable insights into how surface functionalization influences nanocarrier behaviour. While potential heterogeneity introduced by PHA byproducts with multiple acrylate groups is expected to be minimal based on the synthesis process (*40*), their role in structural homogeneity and biodistribution remains an important consideration. Future studies will aim to characterize these byproducts in greater detail to better understand their impact on the system's overall performance.

Finally, the similar biodistribution patterns of NGs in silkworms and mammals further validate the silkworm model as an effective, cost-efficient platform for early *in vivo* evaluation of antimicrobial nanocarriers. This model provides critical insights into cellular interactions and biodistribution, informing the development of future antimicrobial therapies.

Acknowledgements

We thank Sina Hirsch (Würzburg University Hospital) for organizing the international sample shipment and Stephanie Lamer (University of Würzburg) for the LC-MS/MS analysis.

Funding: This work was supported by the German Research Foundation (DFG)-TRR 225 "Biofabrication" (project number 326998133, subprojects A06, B07, B08), DFG-GRK/RTG 2157 "3DInfect" (270563345, subproject P01) and DFG-TRR124 "FungiNet" (210879364, subproject A03). Y. Y. received the Postdoctoral Fellowship for Research in Japan from the Japan Society for the Promotion of Science (JSPS). A. M. received Research Grant by Life Science Foundation of Japan, Research Incentive Grant by The Uehara Memorial Foundation, Team Research Grant by Teikyo University, and JSPS Kakenhi (Grant#22K15461).

Conflict of Interest: Kazuhisa Sekimizu is a consultant for Genome Pharmaceutical Institute, Co., Ltd. The other authors have no conflicts to declare.

References

1. Denning DW. Global incidence and mortality of severe fungal disease. Lancet Infect Dis. 2024; 24:428-438.
2. Bongomin F, Gago S, Oladele RO, Denning DW. Global and multi-national prevalence of fungal diseases-estimate precision. J Fungi. 2017; 3:57.
3. Hossain CM, Ryan LK, Gera M, Choudhuri S, Lyle N, Ali KA, Diamond G. Antifungals and Drug Resistance. Encyclopedia. 2022; 2:1722-1737.
4. Garg A, Sharma GS, Goyal AK, Ghosh G, Si SC, Rath G. Recent advances in topical carriers of anti-fungal agents. Heliyon. 2020; 6:e04663.
5. Zhang X, Malhotra S, Molina M, Haag R. Micro- and nanogels with labile crosslinks – from synthesis to biomedical applications. Chem Soc Rev. 2015; 44:1948-1973.
6. Horvat S, Yu Y, Manz H, Keller T, Beilhack A, Groll J, Albrecht K. Nanogels as antifungal-drug delivery system against *Aspergillus fumigatus*. Adv Nanobiomed Res. 2021; 1:2000060.
7. Vogel T, Kohlmann S, Abboud Z, Thusek S, Fella F, Teßmar J, Sekimizu K, Miyashita A, Beilhack A, Groll J, Yu Y, Albrecht K. Beyond the charge: interplay of nanogels' functional group and zeta-potential for antifungal drug delivery to human pathogenic fungus *Aspergillus fumigatus*. Macromol Biosci. 2024;e2400082.
8. Mouyna I, Dellière S, Beauvais A, Gravelat F, Snarr B, Lehoux M, Zacharias C, Sun Y, de Jesus Carrion S, Pearlman E, Sheppard DC, Latgé JP. What are the functions of chitin deacetylases in *Aspergillus fumigatus*? Front Cell Infect Microbiol. 2020; 10:28.
9. Zamani A, Edebo L, Sjöström B, Taherzadeh MJ. Extraction and precipitation of chitosan from cell wall of zygomycetes fungi by dilute sulfuric acid. Biomacromolecules. 2007; 8:3786-3790.
10. Mitchell MJ, Billingsley MM, Haley RM, Wechsler ME, Peppas NA, Langer R. Engineering precision nanoparticles for drug delivery. Nat Rev Drug Discov. 2021; 20:101-124.
11. Li SD, Huang L. Pharmacokinetics and biodistribution of nanoparticles. Mol Pharmaceutics. 2008; 5:496-504.
12. Zilkowski I, Theodorou I, Albrecht K, Ducongé F, Groll J. Subtle changes in network composition impact the biodistribution and tumor accumulation of nanogels. Chem Commun. 2018; 54:11777-11780.
13. Gracheva I, Konovalova M, Aronov D, Moiseeva E, Fedorov A, Svirshchevskaya E. Size-dependent biodistribution of fluorescent furano-allocolchicinoid-chitosan formulations in mice. Polymers. 2021; 13:2045.
14. Khan M, Yamasta A, Parvin M, Ferdaus J, Ahmed H, Arbab AS. Experimental study of processing of PCL (polycaprolactone)-peptides nanoparticles and its biodistribution analysis for drug delivery system. Micro and Nano Syst Lett. 2024; 12:18.
15. Panthee S, Paudel A, Hamamoto H, Sekimizu K. Advantages of the silkworm as an animal model for developing novel antimicrobial agents. Front Microbiol. 2017; 8:373.
16. Hamamoto H, Urai M, Ishii K, *et al*. Lysocin E is a new antibiotic that targets menaquinone in the bacterial membrane. Nat Chem Biol. 2015; 11:127-133.
17. Nakamura I, Kanasaki R, Yoshikawa K, Furukawa S, Fujie A, Hamamoto H, Sekimizu K. Discovery of a new antifungal agent ASP2397 using a silkworm model of *Aspergillus fumigatus* infection. J Antibiot. 2017; 70:41-44.
18. Lutz J, Yu Y, Wolf AK, Beilhack A, Groll J, Albrecht K. Impact of surface functionality on biodistribution of gold nanoparticles in silkworms. Adv Nanobiomed Res. 2024; 4:2200146.
19. Stichler S, Jungst T, Schamel M, Zilkowski I, Kuhlmann M, Böck T, Blunk T, Teßmar J, Groll J. Thiol-ene clickable poly(glycidol) hydrogels for biofabrication. Ann Biomed Eng. 2017; 45:273-285.
20. Singh S, Zilkowski I, Ewald A, Maurell-Lopez T, Albrecht K, Möller M, Groll J. Mild oxidation of thiofunctional polymers to cytocompatible and stimuli-sensitive hydrogels and nanogels. Macromol Biosci. 2013; 13:470-482.
21. Groll J, Singh S, Albrecht K, Moeller M. Biocompatible and degradable nanogels *via* oxidation reactions of synthetic thiomers in inverse miniemulsion. J Polym Sci Part A Polym Chem. 2009; 47:5543-5549.
22. Zilkowski I, Ziouti F, Schulze A, Hauck S, Schmidt S, Mainz L, Sauer M, Albrecht K, Jundt F, Groll J. Nanogels enable efficient miRNA delivery and target gene downregulation in transfection-resistant multiple myeloma cells. Biomacromolecules. 2019; 20:916-926.

23. Clark KD, Strand MR. Hemolymph melanization in the silkmoth *Bombyx mori* involves formation of a high molecular mass complex that metabolizes tyrosine. J Biol Chem. 2013; 288:14476-14487.
24. Shimabukuro M, Xu J, Sugiyama M, Taniai K, Kadono-Okuda K, Kato Y, Yamamoto M, Chowdhury S, Choi KS, Choi KH, Miyanoshita A, Debnath CN, Yamakawa M. Signal transudation for cecropin B gene expression in adherent hemocytes of the silkworm, *Bombyx mori* (Lepidoptera: Bombycidae). Appl Entomol Zool. 1996; 31:135-143.
25. Matsumoto Y, Sekimizu K. Silkworm as an experimental animal for research on fungal infections. Microbiol Immunol. 2019; 63:41-50.
26. Tansil NC, Li Y, Koh LD, Peng TC, Win KY, Liu XY, Han MY. The use of molecular fluorescent markers to monitor absorption and distribution of xenobiotics in a silkworm model. Biomaterials. 2011; 32:9576-9583.
27. Lavine MD, Strand MR. Insect hemocytes and their role in immunity. Insect Biochem Mol Biol. 2002; 32:1295-1309.
28. Wago H. Humoral factors promoting the adhesive properties of the granular cells and plasmatocytes of the silkworm, *Bombyx mori*, and their possible role in the initial cellular reactions to foreignness. Cell Immunol. 1980; 54:155-169.
29. Longmire MR, Ogawa M, Hama Y, Kosaka N, Regino CA, Choyke PL, Kobayashi H. Determination of optimal rhodamine fluorophore for *in vivo* optical imaging. Bioconjug Chem. 2008; 19:1735-1742.
30. Wyatt GR, Loughheed TC, Wyatt SS. The chemistry of insect hemolymph; organic components of the hemolymph of the silkworm, *Bombyx mori*, and two other species. J Gen Physiol. 1956; 39:853-868.
31. Toutain PL, Bousquet-mélou A. Plasma terminal half-life. J Vet Pharmacol Therap 2004; 27:427-439.
32. Awais MM, Fei S, Xia J, Feng M, Sun J. Insights into midgut cell types and their crucial role in antiviral immunity in the lepidopteran model *Bombyx mori*. Front Immunol. 2024; 15:1349428.
33. Hamamoto H, Horie R, Sekimizu K. Pharmacokinetics of anti-infectious reagents in silkworms. Sci Rep. 2019; 9:9451.
34. Casali A, Batlle E. Intestinal stem cells in mammals and *Drosophila*. Cell Stem Cell. 2009; 4:124-127.
35. Xia X, You M, Rao XJ, Yu XQ. Insect C-type lectins in innate immunity. Dev Comp Immunol. 2018; 83:70-79.
36. Zhang Y, Dong Z, Wang D, Wu Y, Song Q, Gu P, Zhao P, Xia Q. Proteomics of larval hemolymph in *Bombyx mori* reveals various nutrient-storage and immunity-related proteins. Amino Acids. 2014; 46:1021-1031.
37. Ye L, Zhang Y, Dong Z, Guo P, Zhao D, Li H, Hu H, Zhou X, Chen H, Zhao P. Five silkworm 30K proteins are involved in the cellular immunity against fungi. Insects. 2021; 12:107.
38. Fingerhut L, Dolz G, de Buhr N. What is the evolutionary fingerprint in neutrophil granulocytes? Int J Mol Sci. 2020; 21:4523.
39. Eleftherianos I, Heryanto C, Bassal T, Zhang W, Tettamanti G, Mohamed A. Haemocyte-mediated immunity in insects: cells, processes and associated components in the fight against pathogens and parasites. Immunology. 2021; 164:401-432.
40. Steckler R. Phosphate esters of hydroxyalkyl acrylates and hydroxy alkyl methacrylates. Alcolac Inc., U.S., 1974.

Received April 30, 2025; Revised June 10, 2025; Accepted June 21, 2025.

[§] These authors contributed equally to this work.

**Address correspondence to:*
Kazuhisa Sekimizu, Endowed Course "Drug Discoveries by Silkworm Models", Faculty of Pharmaceutical Sciences, Teikyo University, 359 Otsuka, Hachioji, 192-0395 Tokyo, Japan.
E-mail: sekimizu@main.teikyo-u.ac.jp

Krystyna Albrecht, Department for Functional Materials in Medicine and Dentistry, Institute of Functional Materials and Biofabrication, University of Würzburg, 97070 Würzburg, Germany.
E-mail: Krystyna.albrecht@uni-wuerzburg.de